Chapter 2
Hydrogen Trapping and Its Direct Detection

2.1 Manifestations and Analyses of Hydrogen Trapping

2.1.1 Solid Solubility at Low Temperatures

The hydrogen concentration in steel is crucial to the evolution of embrittlement, but its values at failure substantially differ by the steel and the case of failure. The equilibrium hydrogen concentration in steel varies not only by the environment but also by the microstructures of the steel. The main reason is hydrogen trapping in various lattice defects that directly concern the fracture process.

Trapping of hydrogen appears in the temperature dependence of the equilibrium hydrogen content. Observed hydrogen contents are usually of the order of 1 mass ppm in α-iron at room temperature under ordinary environments, far exceeding the solid solubility of hydrogen. Figure 2.1 [1] is the extension of Fig. 1.2 for iron to lower temperatures. Data in the temperature range $1/T > 20 \times 10^{-4}$ substantially scatter, and most specimens are given cold-straining and subsequent annealing that produce various types of lattice defects. Direct measurements of hydrogen solubility are difficult because of very low concentrations at low temperatures. The measurements often utilize hydrogen diffusivity, which is strongly affected by trapping in lattice defects, even weak binding with hydrogen. Permeation techniques are conventional for this purpose, and the following briefly describes the procedure.

The steady-state flow of hydrogen, J_∞, in metal is described by Fick's first law of diffusion,

$$J_\infty = -D_{\mathrm{H}}\frac{\mathrm{d}C}{\mathrm{d}x}, \tag{2.1}$$

where D_{H} is the diffusion coefficient of hydrogen and C is the hydrogen concentration. Assuming Sieverts' law for hydrogen concentrations at the input and output surfaces of the specimen, the total flux j_{t} of hydrogen permeating through a disk of area A and thickness L is expressed in terms of the permeability coefficient Φ as,
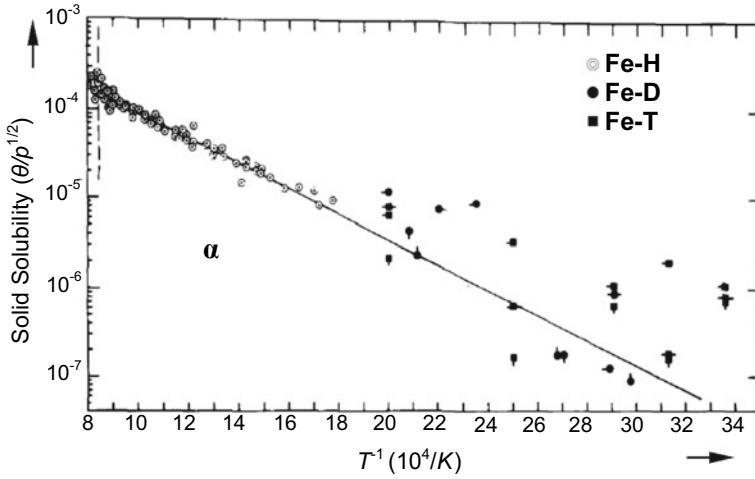
11

Fig. 2.1 Solid solubility of hydrogen in iron in the temperature range from 293 to 1173 K (da Silva et al. [1])

$$j_{\mathrm{t}} = \Phi \frac{A}{L} \left(p_{\mathrm{i}}^{1/2} - p_{\mathrm{o}}^{1/2} \right), \tag{2.2}$$

where p_{i} and p_{o} are pressures in the input and output surfaces, respectively. The numerical value of Φ obtained for α-iron above 373 K is [2]

$$\Phi = (2.9 \pm 0.5) \times 10^{-3} \exp[(-35 \pm 1.8 \mathrm{kJ/mol})/RT], \tag{2.3}$$

where the units of Φ is [cm^3(ntp H$_2$)·cm^{-1}·sec^{-1}·atm$^{-1/2}$].

Electrochemical techniques are also used for hydrogen permeation from the gas phase through sheet specimens [3]. The permeability coefficient for pure iron thus obtained in temperature and pressure ranges of 273–333 K (0–60 °C) and 0.01–1 atm, respectively, is

$$\Phi = 2.6 \times 10^{17} \exp[(-36 \pm 2.5 \ \mathrm{kJ/mol})/RT], \tag{2.4}$$

where the unit of Φ is [atom-H·cm^{-1}·sec^{-1}·atm$^{-1/2}$].

When the hydrogen pressure at the output surface is negligible, the hydrogen concentration at the input surface C_{i} in equilibrium with hydrogen gas of pressure p_{i} is obtained from Eqs. (2.1) and (2.2) using observed Φ and D_{H} as

$$C_{\mathrm{i}} = \frac{\Phi \sqrt{p_{\mathrm{i}}}}{D_{\mathrm{H}}}. \tag{2.5}$$

Equation (2.5) is also applied to the hydrogen entry by cathodic polarization, where C_i [atoms-H·cm^{-3}] is calculated from the steady-state current J_∞ [atoms-H·cm^{-2}·sec^{-1}] as

$$C_i = \frac{J_\infty L}{D_H}. \tag{2.6}$$

Figure 2.2 [4] shows the result of an electrochemical permeation experiment with α-iron single crystal specimens with/without prestraining. Tensile prestrain of 4.3% was given at liquid nitrogen temperature, and the hydrogen concentration was calculated from the steady-state hydrogen flux. The temperature dependence of C_i for specimens without prestrain is consistent with the lower limit of the solubility data in Fig. 2.1 and shows the endothermic nature of the solid solution. On the contrary, the prestrain increases the hydrogen content to a large extent and also changes the hydrogen dissolution from endothermic to exothermic.

The hydrogen concentration C_i in Eqs. (2.5) and (2.6) determined in this way is conventionally termed *diffusible* or *diffusive* hydrogen. It must be careful that C_i is a quantity calculated from the boundary condition of the diffusion equation, and C_i includes hydrogen both in solution and weakly trapped, reversibly to the solid solution to keep local equilibrium. The driving force of diffusion is the concentration gradient of lattice hydrogen, but reversibly trapped hydrogen compensates for the loss of lattice hydrogen by diffusion.

In electrochemical permeation experiments, the electrolyte and the applied cathodic polarization potential control the entry of hydrogen. The condition for electrolysis is crucial not only for the concentration of hydrogen in solution but also for trapped states of hydrogen. In this respect, the effective hydrogen fugacity in electrochemical experiments is a significant quantity. Table 2.1 lists some reported

Fig. 2.2 Temperature dependence of hydrogen content in iron with ($\bigcirc$) and without ($\bullet$) plastic strain of 4.3% (Yamakawa et al. [4]. Reprinted with permission from The Japan Society of Corrosion Engineering)
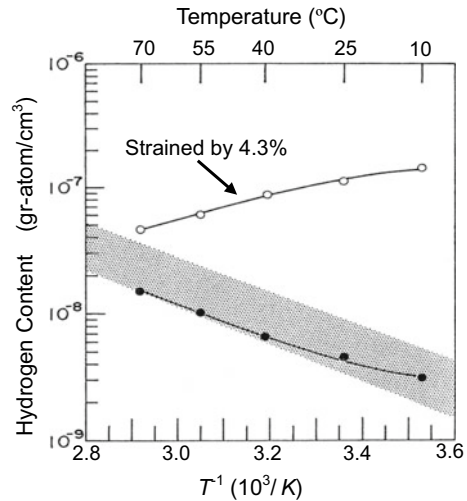
values of hydrogen fugacity for iron and AISI 1045 steel estimated using Eq. (2.2) and permeability coefficients [3, 5].

Under corrosive atmospheric environments, electrochemical reactions on the surface control the hydrogen entry into materials, and the equivalent hydrogen fugacity varies with ambient atmospheres. Figure 2.3 [6] shows records of hydrogen permeation currents for a high-strength Cr–Mo steel foil specimen, the outer side of which is exposed to atmospheric environment. The variation of the permeation current corresponds to daily humidity alternations.

Permeation experiments are used for the measurement of the hydrogen diffusion coefficient that manifests hydrogen trapping. Details of the procedures and thus obtained information are described in Sect. 4.1.2.

Table 2.1 Effective hydrogen fugacity on the surface of electrode at cathodic electrolysis

Materials	Electrolyte	Current density (mA/cm^2)	Hydrogen fugacity (atm)	Hydrogen pressure (atm)
99.5 iron	25 °C, distilled water	–	5.7×10^{-5}	5.7×10^{-5}
Armco iron	25 °C, 0.1 N NaOH	8.1	2.2×10^1	2.2×10^1
99.8 iron	25 °C, 0.1 N H_2SO_4	0.4	5.4×10^2	4.5×10^2
99.9965 iron	24 °C, 1 N H_2SO_4 + 5 g/L As_2O_3	4.5	1.2×10^8	1.8×10^4
99.8 iron	25 °C, 0.1 N NaOH	1.8	1.1×10^0	1.1×10^0
99.8 Ferrovac E	25 °C, 0.1 N NaOH	11.3	2.9×10^1	2.9×10^1
AISI 1045	0.1 N H_2SO_4 + 0.5 mg/L As_2O_3	0.4	$> 1.4 \times 10^4$	
AISI 1045	0.1 N NaOH + 10 mg/L As_2O_3	0–0.6	$0–3 \times 10^3$	

Kumnick et al. [3] and Oriani et al. [5]

Fig. 2.3 Alternating variation of the permeation current density through iron specimen exposed to outer atmospheric environment (Yamakawa et al. [6]. Reprinted with permission from The Iron and Steel Institute Japan)
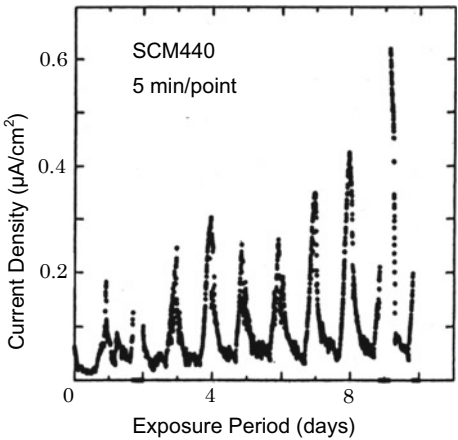
2.1.2 Equilibrium Partition of Hydrogen Among Different Traps

Hydrogen atoms interact with various lattice defects, such as point defects, dislocations, grain boundaries, during migration in the lattice. The potential energy of a hydrogen atom varies by its sites, and the hydrogen atom preferentially stays, i.e., trapped, at sites close to defects where the potential energy is lower than that at interstitial sites in the regular lattice. The binding energy of hydrogen, E_b, with a type of defect is the energy difference between the trapped site and the regular lattice, as shown in Fig. 1.1. The trapping of hydrogen is tighter at sites of higher E_b, making the location more stable.

The total number of trapped hydrogen atoms is the product of the number of sites and the fractional occupancy by hydrogen, and the binding energies with traps determine the distribution of hydrogen atoms. The distribution function for the partition of hydrogen among different sites was discussed by Hirth and Carnahan [7] concerning the adsorption of hydrogen at dislocations and cracks in iron. From a thermodynamics viewpoint, McLellan derived the distribution of hydrogen among trap sites and neighboring regular lattice sites in terms of the Fermi–Dirac distribution, i.e., a maximum of one particle permitted in one state, provided that the fractional occupancy was low and mutual interactions of trapped hydrogen atoms were negligible [8].

The Fermi–Dirac distribution expresses the probability $f(E)$ that a particle will have energy E as

$$f(E) = \frac{1}{1 + \exp[(E - E_F)/k_B T]}, \tag{2.7}$$

where k_B is the Boltzmann constant and E_F is the Fermi energy. Following Beshers [9], the partition of N_H hydrogen atoms in two distinct energy states, E_0 and $E_1 = E_0 - E_b$, under Fermi–Dirac statistics is written as

$$\frac{N_{H0}}{N_0 - N_{H0}} \exp\left(-\frac{E_0}{k_B T}\right) = \frac{N_{H1}}{N_1 - N_{H1}} \exp\left(-\frac{E_1}{k_B T}\right) = \exp\left(\frac{E_F}{k_B T}\right). \tag{2.8}$$

Denoting the state 0 and 1 for the regular lattice and trapped state, respectively, Eq. (2.8) is rewritten in terms of fractional occupancy, θ, as

$$\frac{\theta_x}{1 - \theta_x} = \frac{\theta_L}{1 - \theta_L} \exp\left(\frac{E_b}{k_B T}\right) \approx \theta_L \exp\left(\frac{E_b}{k_B T}\right), \tag{2.9}$$

showing an approximate Boltzmann distribution when $\theta_x \ll 1$. In Eq. (2.9), the sign of the binding energy E_b is changed to negative [9].

The hydrogen occupancy in a trap is higher with tighter binding and higher environmental pressure of hydrogen. Figure 2.4 shows the dependence of the hydrogen

occupancy of the trap, in terms of $C_x = N_{Hx}/N_x$, on E_b and hydrogen pressure at 300 and 500 K for α-iron. The calculation used Eq. (2.9) and θ_L calculated from Sieverts' law. Under constant pressure, log C_x is proportional to E_b for low C_x, and C_x trapped at a site of constant E_b increases with higher pressure or fugacity of environmental hydrogen. However, the linear relationship of log C_x on E_b no longer holds when C_x approaches saturation exceeding *ca.* 0.3 under high pressures.

The ratio of the amounts of hydrogen trapped in sites of different E_b is not constant but varies by environment. From Eq. (2.9), the ratio of θ_x of two trap sites with different E_b is

$$\frac{\theta_{x1}}{\theta_{x2}} = \frac{1 - \theta_{x1}}{1 - \theta_{x2}} \exp\left(\frac{E_{b1} - E_{b2}}{k_B T} \right). \tag{2.10}$$

The environmental dependence of θ_x near saturation differs by E_b, and the ratio is a function of θ_L that varies with the hydrogen fugacity.

In laboratory tests to assess the susceptibility to hydrogen embrittlement, the choice of hydrogen environment, i.e., the hydrogen gas pressure or the electrolyte

Fig. 2.4 Calculated hydrogen occupation of traps in iron with various binding energies under hydrogen gas environments at (**a**) 300 K and (**b**) 500 k. Calculation is conducted using the Fermi–Dirac distribution and the occupation is denoted in terms of the atomic ratio at traps
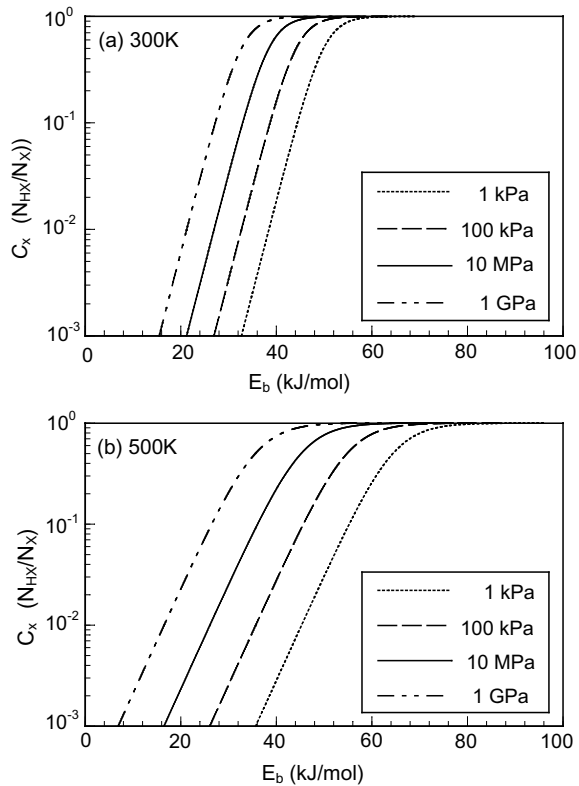
and cathodic potential in electrolysis, is crucial. Introduced hydrogen atoms are distributed among various lattice defects with partitions depending on E_b and θ_L that varies with the hydrogen fugacity present. Hydrogen occupancy is crucial for a defect to operate in the fracture process since embrittlement results from interactions between the defect and hydrogen.

Figure 2.5 shows thermal desorption profiles of hydrogen introduced as a tracer of lattice defects into pure iron [10]. The specimen was first hydrogen precharged and tensile strained to 25% at room temperature. The precharged hydrogen was then degassed at room temperature, and hydrogen was again introduced by cathodic electrolysis. The cathodic electrolysis was mild at a current density of 50 A · m^{-2} for one h in a 0.1 N NaOH aqueous solution with various concentrations of NH$_4$SCN as a catalyst poison. Increasing the amount of poison raises the fugacity of hydrogen.

The desorption rate on the ordinate has two peaks, and the increase in the total amount of desorbed hydrogen appears in the lower temperature peak. The two desorption peaks imply the presence of two types of hydrogen trapping sites of different hydrogen binding energies. Figure 2.5 indicates that the hydrogen occupancy in the trap site composing the higher temperature peak saturates even with the minimum amount of poison. The increase in the lower temperature peak with the amount of poison or hydrogen fugacity indicates an increasing hydrogen occupancy, but the associated shift of the peak temperature suggests that trap sites composing the peak have a range of binding energy.

Discrimination of the type of lattice defect involved in embrittlement is occasionally necessary, but detecting the concerned defect or hydrogen is difficult when the defect's density is substantially low. Reducing hydrogen fugacity is a useful setup to emphasize the preferential partition of hydrogen, provided that the binding energy with hydrogen is high enough. An example is described in Sect. 3.2.3.2 for discriminating hydrogen desorption from vacancy clusters.

Fig. 2.5 Hydrogen desorption spectra and the amounts of tracer hydrogen of H-charged and 25% strained iron. Cathodic H-charging was in 0.1 N NaOH aq. with various NH$_4$SCN concentrations (Sugiyama et al. [10])
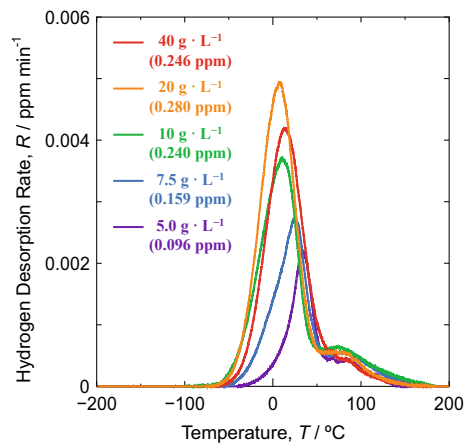
2.1.3   Kinetics of Hydrogen Trapping

The progress of hydrogen occupancy in traps is not the same by the type of trap but depends on the E_b of each trap. Hydrogen atoms tolerate trapping and de-trapping in lattice defects during migration, and the transient hydrogen partition among various defects differs from that in equilibrium, as stated in the previous section. Detecting trapped hydrogen in a specific defect is not straightforward, and the hydrogen thermal desorption analysis (TDA) is a conventional method described in Sect. 2.2.1. Hydrogen desorbed under a controlled temperature ramp generally exhibits multiple desorption-rate peaks, and hydrogen desorption from traps of higher E_b generally shifts to higher temperatures.

Figure 2.6 [11] shows areas of the two peaks in TDA profiles of a eutectoid steel cold-drawn by 75% and subjected to sustained loading in a 20% NH_4SCN aqueous solution at 323 K under an applied stress of 0.5 of the ultimate tensile strength. The thermal desorption profile of the steel exhibited two peaks. Still, their evolution was of an entirely different origin, due to materials and hydrogen-charging conditions, as shown in Fig. 2.5 for pure iron. The ordinate of Fig. 2.6 denotes the amount of hydrogen absorbed during immersion, measured as the intensity or the area of the desorption peaks. Small peak 2 locates at a higher temperature than peak 1, implying a higher E_b than that for peak 1. The faster reach to saturation of the higher temperature peak than the lower temperature peak, in Fig. 2.6, implies faster occupancy in sites of higher E_b.

Transient occupation also proceeds in hydrogen permeation experiments. The fundamental equation of diffusion is classical Fick's second law. The equation is for diffusion in a uniform media, and McNabb and Foster modified the equation, including trapping and de-trapping during migration [12]. McNabb–Foster equation is of the form,

Fig. 2.6 Amount of desorbed hydrogen from cold-drawn eutectoid steel wires subjected to the FIP test for increasing periods. The reduction of specimens at cold-drawing is 75% (Takai et al. [11]. Reprinted with permission from The Iron and Steel Institute Japan)
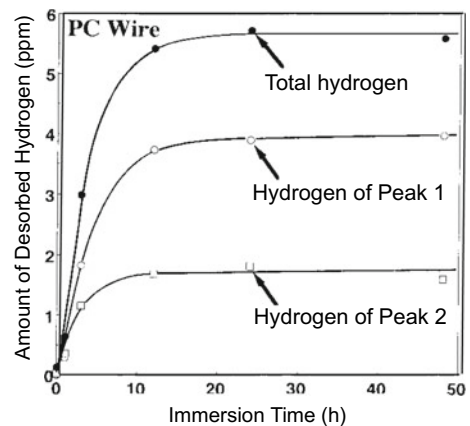
$$\frac{\partial C_L}{\partial t} + \sum_i N_i \frac{\partial \theta_i}{\partial t} = D_L \nabla^2 C_L, \tag{2.11}$$

with

$$\frac{\partial \theta_i}{\partial t} = k_i C_L (1 - \theta_i) - p_i \theta_i, \tag{2.12}$$

where the hydrogen concentration C, the numbers of hydrogen atoms per unit volume of the lattice N_L, and x-trap site N_x are related to the fractional occupancy θ as

$$C_L = N_L \theta_L, \tag{2.13}$$

and

$$C_x = N_x \theta_x. \tag{2.14}$$

It is to be noticed that N includes the coordination number available for hydrogen around one lattice or defect site of host metals. In Eq. (2.12), k and p are trapping- and de-trapping-rate parameters. The terms $k_i C_L (1 - \theta_i) N_i$ and $p_i \theta_i N_i$ are numbers of hydrogen atoms captured at and released from the ith trap in unit volume per second. Details of diffusion equations are described in Sect. 2.2.1 concerning TDA.

Kasuya and Fuji calculated transient changes of hydrogen content in two classes of traps for the hydrogen permeation from one side and the desorption from both sides of a plate specimen [13]. The traps were characterized by the magnitude of $N_i k_i / p_i$ of 20 and 3, respectively, as the first and second classes of traps, i.e., deeper trapping in the first class, while Nk was the same for the two classes. Kasuya and Fujii assumed an exponential-form time dependence of trapped hydrogen concentration common to the two classes and numerically solved Eqs. (2.11) and (2.12) to calculate hydrogen distributions along the thickness of the plate. Figure 2.7 plots calculated trap hydrogen concentrations, C_i, at the i-th trap located at the center of the plate of thickness a. The elapsed time is normalized by $D_L t / a^2$, where D_L is the hydrogen diffusion coefficient in the lattice, and a is the plate thickness. C_is were normalized by the initial trap hydrogen concentrations, $C_{i,0}$, in (a) and by the steady boundary hydrogen concentrations, $C_{i,x\infty}$ in (b), respectively. The lower Nk/p of 20 for the class 1 of trap implies tighter hydrogen trapping than the class 2. However, for the permeation shown in Fig. 2.7a, the build-up of the hydrogen concentration in class 1 is slower than in class 2, contrary to the TDA result in Fig. 2.6.

When multiple traps are present, experimental and theoretical studies about the hydrogen partition and its kinetics are scarce. Failure in hydrogen embrittlement starts as a local event, and local hydrogen behaviors and the concerned site are crucial subjects for materials design against hydrogen embrittlement.
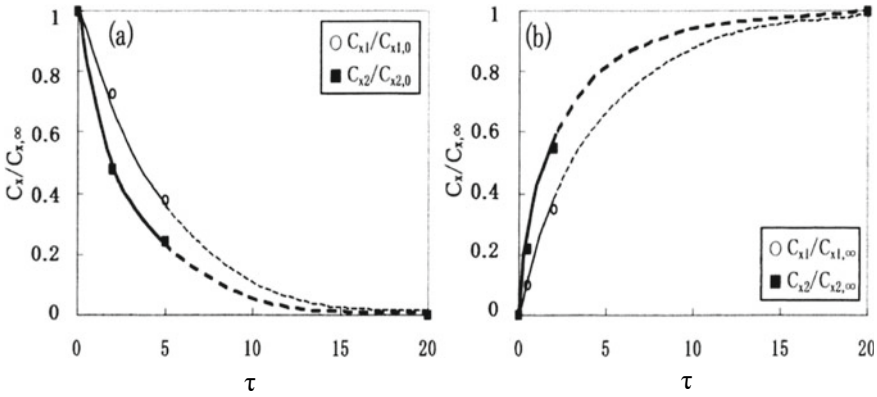
Fig. 2.7 Calculated time dependence of trap hydrogen concentrations. **(a)** Desorption and **(b)** build-up at two classes of traps located at the center of plate specimen. $\circ$ and $\blacksquare$ denote Class 1 and Class 2, respectively, each Nk/p being 20 and 3. τ is the normalized time by $D_L t/a^2$. Plots of calculated results in Ref. [13]

2.2 Detection of Hydrogen Trapping and Distribution

2.2.1 Hydrogen Thermal Desorption Analysis

2.2.1.1 Principles of TDA

Analyses of the desorption of adsorbed gases from the metal surface under a controlled temperature ramp provide information on various parameters such as the number, populations of adsorbing phases, and the activation energy of desorption [14]. The thermal desorption spectroscopy (TDS) developed for characterizing adsorbed gases on the surface of materials has been applied to hydrogen diffusing out from bulk specimens of metals [15–17]. The activated de-trapping and decreased trapped hydrogen concentration, associated with the temperature rise, form a desorption-rate peak on the TDA profile. The desorption-rate profile against temperature is affected not only by hydrogen states in the metal but also by experimental parameters such as the specimen size and the temperature-ramp rate. Accordingly, the terminology thermal desorption analysis (TDA) is more appropriate than TDS for analyzing hydrogen states in metals.

In TDA, the measured quantity is the desorption rate of lattice hydrogen that diffuses through the material undergoing trapping and de-trapping processes. The rate-determining process of desorption during the temperature ramp differs by trapped states of hydrogen. When trapping is weak and local equilibrium exists between lattice and trapped hydrogen, thermally activated diffusion through lattice is the rate-determining with a diffusion coefficient that depends on the density of and the binding energy with reversible trap sites. On the other hand, when trapping is pretty strong, the thermally activated dissociation of trapped hydrogen with elevating

temperature is the rate-determining desorption process. Usually, desorption of tightly trapped hydrogen occurs at high temperatures, but the distinction between the two extreme processes is not simple and careful examinations of TDA are necessary.

Figure 2.8 [18] shows TDA profiles of hydrogen introduced to eutectoid steel, the material used in Fig. 2.6, cold-drawn to various reductions of area. Hydrogen was introduced by immersing the steel wires of 5 mm in diameter in a 20% NH₄SCN aqueous solution at 323 K for 24 h, and the heating rate of TDA was 200 K/h. The specimen without cold-drawing shows a single desorption-rate peak with the peak temperature at about 420 K. The amount of desorbed hydrogen increased with increasing reductions on cold-drawing, and an additional desorption peak appeared at higher temperatures. The increase initially appeared in TDA profiles for the lower temperature peak and successively for the higher temperature one. For simplicity, the term "desorption peak" or simply "peak" is occasionally used hereafter instead of "the desorption-rate peak".

Hydrogen states corresponding to the two peaks are substantially different. For the TDA of the specimen cold-drawn by 85%, the lower temperature peak almost disappeared after exposing the specimen at room temperature for two weeks, indicating that hydrogen composing the lower temperature peak is diffusive. On the contrary, the higher temperature peak was hardly affected by room temperature exposure, indicating the non-diffusive nature of trapped hydrogen.

For pure iron, the hydrogen absorption capacity increases by cold-drawing, with only a single desorption-rate peak at about 400–500 K, depending on the specimen's size [17]. The peak disappears when hydrogen-charged specimens are exposed at room temperature, indicating the diffusive nature of hydrogen. It should be careful that a seemingly single peak in a TDA profile occasionally involves the desorption of hydrogen from various weakly trapped lattice defects in the ferrite phase, as described in Fig. 3.5. On the other hand, trap sites of non-diffusive hydrogen that composes the higher temperature peak in Fig. 2.8 for cold-drawn eutectoid steels must be created by heavy deformation of eutectoid cementite, but the entity of trapping is not definite.

Fig. 2.8 Thermal desorption curves of hydrogen introduced to eutectoid steel specimens cold-drawn to various reductions of area RA (Takai et al. [18])
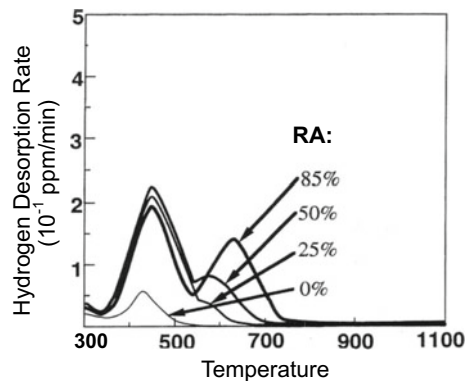
The evolution of separate peaks implies different types of rate-controlling processes in hydrogen desorption.

2.2.1.2 Dissociation-Controlled Desorption

The quantities that describe hydrogen trapping are the density of the trap site, hydrogen occupancy therein, and hydrogen binding energy E_b. There exist some procedures to estimate these quantities from TDA.

Kissinger expressed the reaction rate of thermal dissociation of minerals, e.g., solid $\rightarrow$ solid $+$ gas, in the form [19]

$$\frac{dX}{dt} = A(1 - X)^n \exp\left(-\frac{E_a}{RT}\right), \tag{2.15}$$

where X is the fraction reacted, A is the reaction constant, n is the order of the reaction, and E_a is the activation energy of the reaction. This equation was applied to the thermal desorption of gases from metal surfaces [14] and the thermal de-trapping of hydrogen from trap sites in metals [15].

The peak temperature T_p at which the dissociation rate is maximum is obtained by differentiating Eq. (2.15) with t as,

$$\frac{d}{dt}\left(\frac{dX}{dt}\right) = \frac{dX}{dt}\left[\frac{\varphi E_a}{RT^2} - A\exp\left(-\frac{E_a}{RT}\right)\right] = 0, \tag{2.16}$$

or

$$\frac{\varphi E_a}{RT_p^2} = A\exp\left(-\frac{E_a}{RT_p}\right), \tag{2.17}$$

for a reaction of the first order ($n = 1$) and a linear heating rate of

$$T = T_0 + \varphi t. \tag{2.18}$$

Differentiation with $1/T_p$ of the logarithm of Eq. (2.17) gives.

$$\frac{\partial \ln(\varphi/T_p^2)}{\partial(1/T_p)} = -\frac{E_a}{R} \tag{2.19}$$

Then, the activation energy of de-trapping, E_a, is obtained from the gradient of the plot of $\ln\left(\varphi/T_p^2\right)$ versus ($1/T_p$), using measured T_p at various heating rates.

Figure 2.9 is an example of applying Eq. (2.19) to obtain E_a [20]. The material was low-carbon steel tensile strained 25% at 223 K. Tritium, instead of hydrogen, was introduced by cathodic electrolysis in a 1 N NaOH aqueous solution with a

Fig. 2.9 Arrhenius plot of the peak temperatures by changing the heating rate, φ, for iron specimens strained by 25% at 223 K (Nagumo et al. [20])
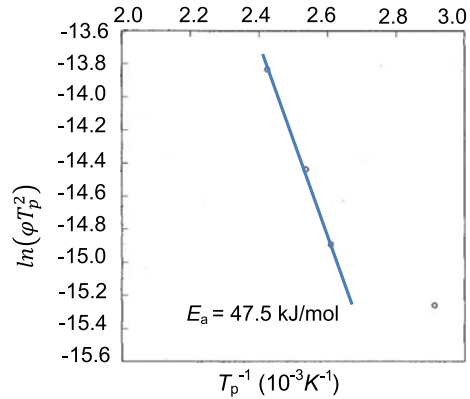
current density of 50 A/m^2. The condition was substantially mild, and the measure of the amount of desorbed tritium was radioactivity. The TDA profile had a single desorption-rate peak with T_p varying about 70 K around 380 K by the heating rate. A linear Arrhenius relation was satisfactory, giving an E_a of 47.5 kJ/mol when the data point corresponding to the lowest heating rate was excluded. In this experiment, the amount of absorbed tritium increased with the given tensile strain, but the strained materials almost lost the tritium absorption capacity when annealed at 473 K. The result implied that lattice defects in the ferrite matrix acting as the trap site of tritium were vacancies rather than dislocations.

It must be careful that the method stated above to evaluate E_a is valid, provided that the desorption is rate-limited by the dissociation of trapped hydrogen rather than by lattice diffusion of hydrogen. The condition is proper for detecting tightly trapped hydrogen, and a measure of the applicability is the magnitude of E_b. However, the exact determination of the critical magnitudes of E_a at the border of reversible or irreversible traps is difficult. The suggested values are 26.4 kJ/mol for E_a by Lee and Lee [16] and 64 kJ/mol for E_b by Oriani [21] for iron at room temperature. The experimentally determined E_a of the higher temperature peak in Fig. 2.8, according to Eq. (2.19), was 65 kJ/mol [22].

Turnbull et al. conducted a more rigorous treatment [23], and they noticed that the application of Kissinger's equation, Eq. (2.15), is valid for low lattice hydrogen contents and a very low trap occupancy, as described in Sect. 2.2.1.4. An experimental method to check whether the desorption is dissociation-controlled or not is the dependence of TDA profiles on the specimen size. For the dissociation-controlled desorption, TDA profiles are unaffected by the specimen size since A in Eq. (2.15) is a constant irrelevant to the specimen size.

When hydrogen binding energies with traps are substantially high and the desorption is dissociation-controlled, multiple peaks are to appear in the TDA profile, corresponding to desorption from each trap.

2.2.1.3 Diffusion-Controlled Desorption

On the other hand, when hydrogen diffusion in metals limits the desorption rate, parameters of hydrogen trapping are estimated by modeling TDA profiles. Fundamental diffusion theories are described in Sect. 4.1.3, and here are some examples of the use of trapping parameters for modeling TDA profiles.

The diffusion coefficient incorporates trapping and de-trapping effects during hydrogen migration. Weakly trapped hydrogen is reversible to lattice, involved in diffusing hydrogen. Fick's first diffusion law, Eq. (2.1), for the flow of lattice hydrogen is applied to the total hydrogen concentration C_T that includes trapped hydrogen in equilibrium with lattice hydrogen. An idea of the diffusion equation when trapped states are present is to introduce the "effective hydrogen coefficient D_{eff}" in Fick's law, as

$$J = -D_{eff}\frac{dC_T}{dx}. \tag{2.20}$$

Oriani expressed D_{eff} considering equilibrium between atomic populations in the regular lattice and traps [21]. When hydrogen occupies a fraction θ of available sites, the equilibrium constant K is the ratio of the activity of hydrogen in the trap sites to that in lattice sites. For very low C_L, i.e., $\theta_L \ll 1$, K in terms of the fractional occupancy is in the form of

$$K = \frac{1}{\theta_L}\left(\frac{\theta_x}{1-\theta_x}\right), \tag{2.21}$$

where suffices x and L denote trapping and normal lattice sites, respectively. The local equilibrium that Oriani assumed was that change in the lattice hydrogen concentration is compensated in the same time interval by the same amount of trapped hydrogen to keep equilibrium.

The hydrogen concentration C, defined as the number of hydrogen atoms per unit volume, is the product of the number of sites per unit volume, N, and the fractional occupancy, θ, thereof, i.e.,

$$C_L = N_L\theta_L, \tag{2.22}$$

and

$$C_x = N_x\theta_x, \tag{2.23}$$

N includes the coordination number available for hydrogen around one lattice or defect site of host metals.

Comparing Eqs. (2.1) and (2.20) of Fick's first law, D_{eff} relates to the normal diffusivity D_L and trapping parameters in Eqs. (2.21)–(2.23) in the form of

$$D_{\text{eff}} = D_{\text{L}} \frac{dC_{\text{L}}}{dC_{\text{T}}} = D_{\text{L}} \left[1 + \frac{N_x N_{\text{L}} K}{(N_{\text{L}} + K C_{\text{L}})^2} \right]^{-1} \tag{2.24}$$

$$= D_{\text{L}} \frac{C_{\text{L}}}{C_{\text{L}} + C_x(1 - \theta_x)}. \tag{2.25}$$

For $\theta_x \ll 1$, i.e., for very low occupancy of trapping sites,

$$D_{\text{eff}} = D_{\text{L}} \frac{C_{\text{L}}}{C_{\text{T}}}. \tag{2.26}$$

When C_{L} is very small, D_{eff} in Eq. (2.24) is written in terms of the density of trap sites, $\Gamma_x (= N_x/N_{\text{L}})$, and the binding energy E_{b} as

$$D_{\text{eff}} = D_{\text{L}} \left[1 + \Gamma_x \exp\left(\frac{E_{\text{b}}}{RT} \right) \right]^{-1}. \tag{2.27}$$

Ono and Meshii considered dynamic equilibrium between trapping and de-trapping processes and obtained an expression of D_{eff} similar to Eq. (2.27), taking into account the entropy factor [17]. The desorption rate is calculated from the solution of Fick's second law of diffusion,

$$\frac{\partial C}{\partial t} = D \frac{\partial^2 C}{\partial x^2}, \tag{2.28}$$

with proper initial and boundary conditions. Ono and Meshii simulated TDA profiles of quenched-in hydrogen from high temperatures in pure iron specimens [17]. Observed TDA profiles showed a single desorption peak at about 420 K, excluding an artifact peak at 220 K due to the desorption of water molecules from the metal surface. Computations using a finite difference method gave simulated TDA profiles coincident with observed ones using D_{eff} with $E_{\text{b}} = 51$ kJ/mol and $\Gamma_x = (4\text{--}15) \times 10^{-5}$ in Eq. (2.27).

In the case of weak traps, Yamaguchi and Nagumo examined the effects of trapping parameters in TDA profiles using D_{eff} [24]. The specimens were martensitic steel plates, and experimental variables were the plate thickness, the amount of prestrain to vary the density of defects, the hydrogen-charging time to vary the initial distribution of hydrogen in specimen, and the heating rate. Hydrogen as a tracer of lattice defects was introduced to the deformed specimen by substantially mild cathodic electrolysis using a 3% NaCl + 3 g/l NH$_4$SCN aqueous solution at a current density of 5 A/m^2. The mild condition prevented to induce of extraneous defects by cathodic electrolysis. TDA profiles were simulated using Eq. (2.28) with D_{eff} defined by Eq. (2.27), including Γ_x and E_{b} as fitting parameters.

Figure 2.10 [24] compares observed and simulated TDA profiles for specimens of 2 mm in thickness with increasing heating rates. For the calculation, assumed Γ_x and E_{b} were 8.5×10^{-2} and 17 kJ/mol, respectively. Figure 2.11 [24] also compares

observed and simulated TDA profiles for specimens given different amounts of strain. The calculation assumed constant E_b at 20 kJ/mol and varied Γ_x.

The peak temperature T_p at which the desorption rate is maximum shifts to higher temperatures with increasing E_b, as shown in Fig. 2.12(a) [24], but T_p is also a function of Γ_x as shown in Fig. 2.12(b) [24]. Accordingly, modeling an observed T_p cannot uniquely determine the proper combination of Γ_x and E_b. Another measure of proper fitting is the desorption-rate peak width. The peak width at the same T_p is broader when calculated using larger Γ_x and smaller E_b values. A proper characterization of TDA profile in addition to T_p is necessary for utilizing modeling to estimate trapping parameters. It is also to be noticed that specimen geometries affect TDA profiles in the case of diffusion-controlled desorption.

TDA gives useful information on lattice defects that affect hydrogen-related failure, but one should be aware that an exact estimation of trapped states of hydrogen is not straightforward in the case of diffusion-controlled desorption.

Fig. 2.10 Thermal desorption curves of hydrogen from martensitic steel specimens of 2 mm in thickness at various heating rates. **(a)** Experimental curves, **(b)** simulation curves (Yamaguchi et al. [24])
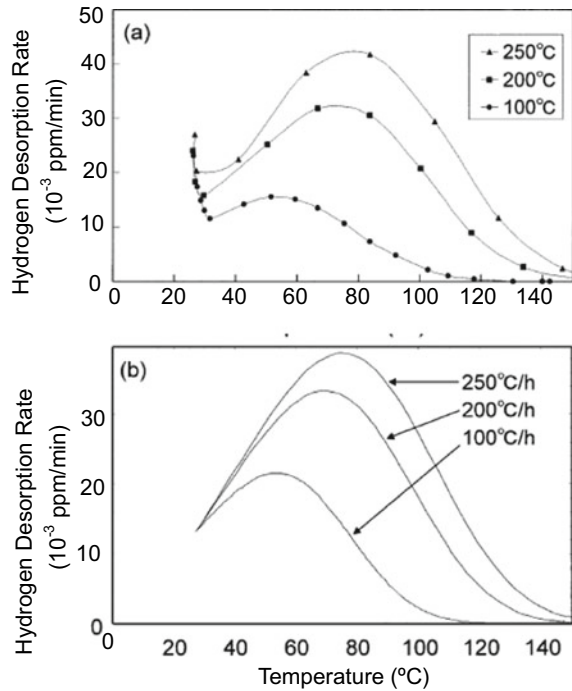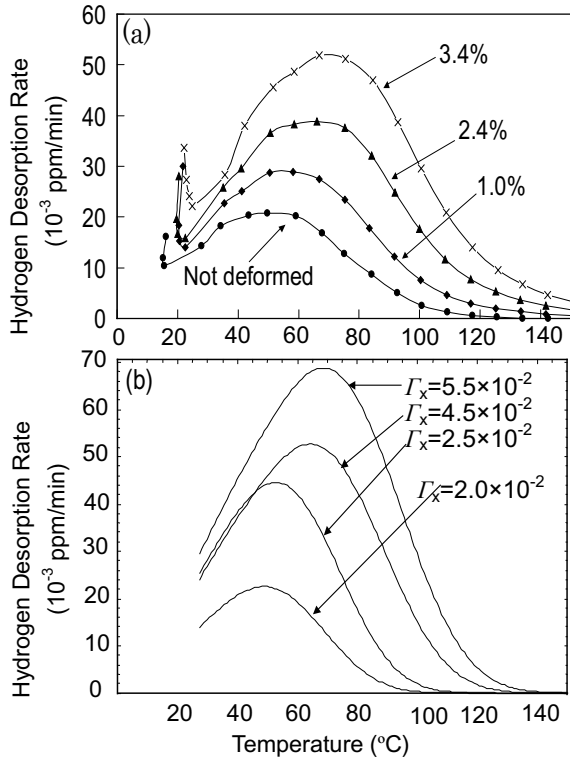
Fig. 2.11 Thermal desorption curves of hydrogen from martensitic steel specimens of 2 mm in thickness given various amounts of strain. **(a)** Experimental curves, **(b)** simulation curves for traps of the binding energy of 20 kJ/mol and different densities Γ_x. The heating rate is 100 °C/h (Yamaguchi et al. [24])

2.2.1.4 Simulation of TDA Profile with Multiple Peaks

Desorption peaks in TDA often exhibit asymmetry, accompanying broadening of the width and the presence of hump(s) or sub-peak(s). Such features manifest the existence of multiple types of traps. The McNabb–Foster equation for the hydrogen diffusion accompanying trapping processes is Eqs. (2.11) or (2.12) in Sect. 2.1.3. Trapping and de-trapping are thermally activated processes, and k and p in the McNabb–Foster equation are related to potential energies shown in Fig. 2.13. Expressions of k and p are [23]

$$k = k_0 \exp\left(-\frac{E_t}{RT}\right),$$
$$p = p_0 \exp\left(-\frac{E_b + E_t}{RT}\right). \tag{2.29}$$

In Fig. 2.13, the change in the saddle point energy ΔE is either positive or negative according to the relative magnitude of E_t and E_m. Parameters p and k are not independent. When the occupation of hydrogen in the trap is low enough, the ratio k/p

Fig. 2.12 Effects of **(a)** the binding energy with hydrogen and **(b)** the density of the trap on simulated thermal desorption curves. **(a)** The trap density is fixed at 1.0×10^{-4}, **(b)** the binding energy is fixed at 58.6 kJ/mol. The plate thickness is 2 mm, and the heating rate is 100 °C/h (Yamaguchi et al. [24])
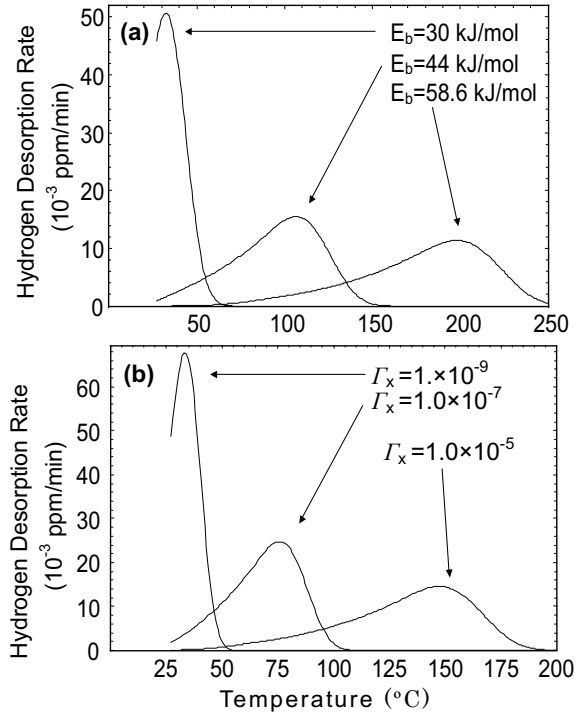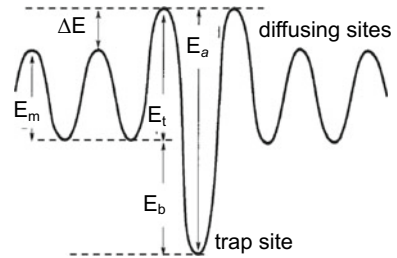
Fig. 2.13 Schematic illustration of energy states of hydrogen in lattice and trap sites in metals

in the steady-state condition ($\partial\theta/\partial t = 0$) gives

$$\frac{k_0}{p_0} = \frac{1}{N_L(1-\theta)} \approx \frac{1}{N_L} = \text{constant} \tag{2.30}$$

The general solution of the McNabb–Foster equation, Eqs. (2.11) and (2.12), is difficult. McNabb and Foster derived an approximate solution for thick specimens, i.e., the case where frequent trapping and de-trapping occur during diffusion under dynamic equilibrium between trapped and lattice hydrogen, i.e., equal numbers of trapping and de-trapping per unit time [12]. When the hydrogen concentration is low enough, McNabb–Foster's equation Eq. (2.11) is reduced to the form of Fick's

second law by using D_{eff} defined as

$$D_{eff} = D_L \left(1 + N_x \frac{k}{p}\right)^{-1}. \tag{2.31}$$

Equation (2.31) is a kinematic expression of D_{eff} used by Oriani, Eq. (2.27), derived under the local equilibrium concept. Descriptions of the hydrogen diffusion process are also described in Sect. 4.1.3 concerning permeation experiments.

TDA profiles are affected by parameters characterizing trap sites, as described in the previous section. Turnbull et al. simulated TDA profiles by solving the McNabb–Foster equation, Eqs. (2.11) and (2.12), using a finite differential method [23]. The ratio k/p is vital in the analysis. Since the functional form of D_{eff} in Eq. (2.31) is similar to that in Eq. (2.28), calculated TDA profiles obtained using Eqs. (2.27) and (2.31) are similar. For the case of a single trap, key material variables that determine the TDA profile are the density of trap sites and the binding energy. Their effects are similar to those shown in Figs. 2.10 and 2.11 obtained using the effective diffusivity. The peak hydrogen flux and the peak temperature have no marked dependence on the magnitude of the rate constants k_0 and p_0 [23].

Impacts of test parameters such as the heating rate and the sample thickness are also similar between the two modeling methods [23, 24]. The increase in C_0 enhances the desorption in the lower temperature side of the peak and shifts the desorption peak to a lower temperature [24]. An explanation is that the higher C_0 causes the higher occupancy of traps and reduces the retrapping of diffusing lattice hydrogen, resulting in faster diffusion at lower temperatures.

Turnbull et al. extended their calculations to the case of two types of traps [23], i.e., $i = 1$ and 2 in Eq. (2.11). The calculated TDA profile for two traps with binding energies of 48 and 68 kJ/mol exhibits two discrete peaks, and each peak is the same as the one expected for the case of a single trap of 48 or 68 kJ/mol in the binding energy. However, when binding energies are closer, e.g., 48 and 58 kJ/mol, the two peaks merge into one peak. In the calculation, the densities of the two traps are assumed to be the same. The appearance of discrete peaks should depend not only on the difference in the binding energies but also on their magnitudes and the densities of traps.

Enomoto et al. simulated TDA profiles using a finite difference method to solve the McNabb–Foster equation [25]. The observed TDA profile of hydrogen from martensitic steel showed a single peak, and Enomoto et al. assumed hydrogen trapping in the elastic strain field of dislocations. In their analyses, the binding energy of 27 kJ/mol and the density of trap sites were assumed from the literature, and the fractional occupancy was estimated from the observed amount of hydrogen. Trapping and de-trapping parameters in Eq. (2.29) were determined to match the calculated peak temperature and desorption rate to the observed ones. The determined ratio p_0/k_0 of the order of $10^{29}/m^3$ is nearly coincident with the values employed by Turnbull et al. [23]

Fig. 2.14 Simulation of TDA profiles in Fig. 2.8, showing the influence of the binding energy E_b of interfacial trapping sites on Peak 2. After the appearance of Peak 2, its shift does not affect the height and the temperature of Peak 1 (Ebihara et al. [26]. Reprinted with permission from The Iron and Steel Institute Japan)
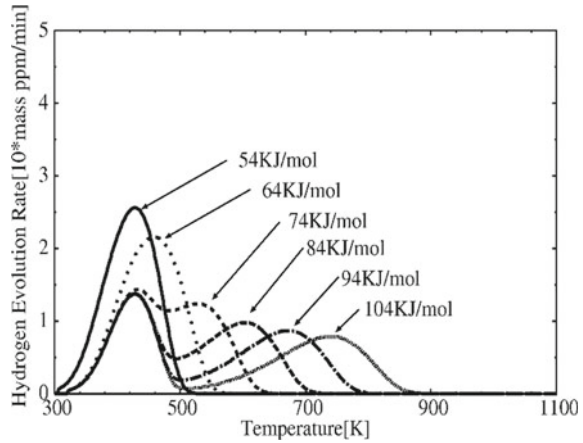
Enomoto et al. also simulated TDA profiles that exhibited two desorption-rate peaks, in Fig. 2.8, for a cold-drawn eutectoid steel bar specimen [25]. They presumed the elastic strain field and dislocation core as the trap sites of the two peaks and used each binding energy of 27 and 50 kJ/mol, respectively, in the literature. The trap densities and the initial fractional occupancies of the traps were estimated by assuming the dislocation density of 10^{16} m^{-2} and observed hydrogen fluxes of the two peaks. A formerly determined p_0/k_0 value for martensitic steel was also used. A part of hydrogen introduced into the specimen diffused out during room temperature exposure, and the simulation satisfactorily reproduced the observed decay of the lower temperature peak in TDA profiles. However, it must be careful that a set of parameters is not unique to a given TDA profile. Justification of presumed assignments of trap sites to microstructures is a separate issue.

On the other hand, Ebihara et al. proposed a numerical model to simulate the TDA profile [26], combining the McNabb–Foster equation and Oriani's local equilibrium theory. They assumed fast hydrogen diffusion in the lattice and local equilibrium in trap sites at each time-step of the temperature ramp. The amount of hydrogen desorption is the whole hydrogen removed from the interstitial site at each step. The application of their model to the TDA profile shown in Fig. 2.8 is Fig. 2.14, in which E_b of the trap site forming the higher temperature peak is employed as a parameter [26].

2.2.1.5 Some Technical and Intrinsic Problems of TDA

(a) LTDS

TDA is a powerful tool for investigating trapped states of hydrogen in metals, but the analyses, described above, have some limitations in identifying trapped states of hydrogen. In conventional TDA procedures, a substantial amount of hydrogen is lost
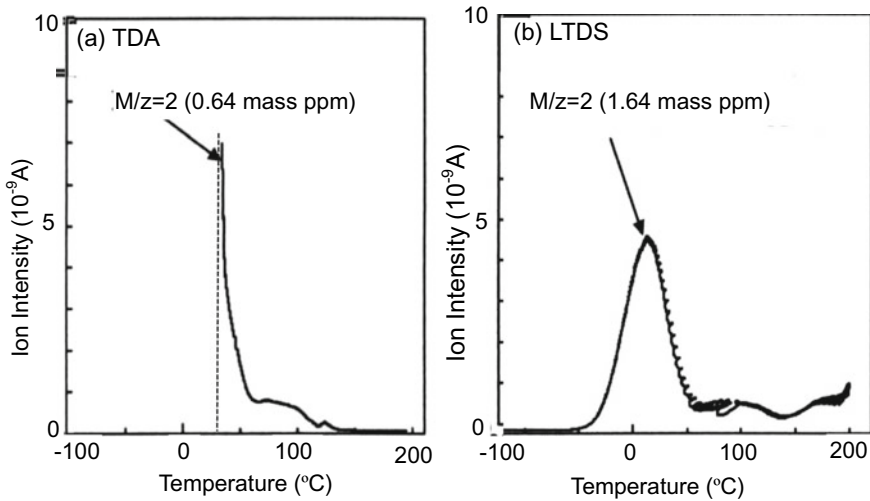
Fig. 2.15 Comparison of TDA and L-TDS curves of hydrogen from 90% cold-rolled iron specimens of 0.5 mm in thickness. Hydrogen is charged by immersing the specimens in 20% NH$_4$SCN aq at 50 °C for 24 h (Sato et al. [27]. Reprinted with permission from The Iron and Steel Institute Japan)

prior to the start of the temperature ramp. A device to avoid the difficulty is the low-temperature thermal desorption spectroscopy (LTDS), which starts the temperature ramp from a temperature as low as 70 K [10, 27, 28].

LTDS correctly measures early parts of hydrogen desorption in the low diffusivity range without an inevitable loss of hydrogen that happens in conventional TDA. LTDS enables the complete form of TDA profile, as exhibited in Fig. 2.15 [27], comparing conventional TDA and LTDS profiles of hydrogen introduced into a plastically deformed pure iron specimen of 0.5 mm in thickness. Examples of LTDS are also shown in Figs. 2.5 and 3.11.

(b) Determining trapping parameters

In the McNabb–Foster equation, the trapping parameters, *k* and *p,* are mostly used for modeling with their ratio, *k/p,* and Pound et al. devised a method to separate the parameters [29]. On electrochemical permeation, a devised method was double-step to introduce hydrogen into the metal specimen, firstly at a cathodic potential for a short time and then to step-up the potential to a more positive value to remove diffusive hydrogen. The amount of removed hydrogen was counted as the anodic charge from the transient anodic current, and the difference between the total charge passed into the metal and the charge passed out during the discharge gave the amount of irreversibly trapped hydrogen.

It was assumed that the change of hydrogen concentration with time was due to the diffusional flow and the capture in irreversible traps. The trapping-rate parameter, κ, was defined as

$$\kappa = kN_x(1 - \theta_x), \tag{2.32}$$

including trapping parameters k and N_x defined in Eq. (2.12). Experiments conducted for iron in aqueous H_2S solutions gave the values of κ of 0.25 s^{-1} that decreased to 0.05 s^{-1} by annealing, but the nature of the irreversible trap sites was not definite.

(c) Limitations

TDA presumes that the microstructures of the material are unaltered during the measurement, except for the release of hydrogen. However, the temperature ramp occasionally alters defect structures in materials, and microstructures of steel are not always thermally stable as envisaged in the tempering of martensite or recovery of plastically strained materials. Thermal desorption of hydrogen occurs not only by the activated diffusion or thermal release from traps but also is associated with alterations of trapping defects themselves, such as precipitation of carbides, reconfiguration of dislocations, and annihilation of point defects. However, analysis of the TDA profile taking into account such structural alterations during temperature ramp has not been established.

Another point to be considered associated with the temperature ramp is the properness of the local equilibrium condition. The hydrogen binding energy with traps is a major factor determining the desorption rate. A local equilibrium as a premise for diffusion-controlled desorption is viable for E_b lower than a border value. However, the border value is a function of temperature [21], and the rate-controlling process for desorption occasionally alters during the temperature ramp. Such situations impose difficulties in selecting accurate approximations for the analyses. In the case of diffusion-controlled desorption from multiple types of traps, separating respective traps is difficult when hydrogen in each trap is in local equilibrium with lattice hydrogen. LTDS is a device to improve the analysis' precision and to separate desorption peaks arising from traps with close E_b. The separation of weakly trapped states of hydrogen using LTDS is presented also in Sects. 3.1.1.3 and 3.2.3.2. However, hydrogen partitions at various trap sites change during the temperature ramp, and modeling of observed LTDS profiles has not yet been conducted.

TDA gives valuable information about microstructures and lattice defects relevant to hydrogen. However, it is again to be noticed that trapping parameters estimated from a TDA profile, such as the binding energy and the trap density, do not straightly indicate microscopic entities of the trap. In many cases, TDA results are utilized in the context of consistency with otherwise estimated lattice defects relevant to hydrogen. TDA gives information averaged over the entire specimen, while the material fracture is a local event to be studied in various ways.

2.3 Visualization of Hydrogen Distribution

The distribution of hydrogen in materials is not uniform, and microstructural inhomogeneities and lattice defects are preferential sites for hydrogen atoms to locate.

Revealing the sites where hydrogen actively interacts is crucial to elucidate the local events operating in embrittlement and for the design of materials. Direct observation of hydrogen atoms is favorable, but the weak response of hydrogen atoms to external excitations and their high mobility impose technical difficulty. Some methods are presented here.

### 2.3.1 Tritium Autoradiography and Hydrogen Microprint Technique

Tritium is a radioactive isotope of hydrogen, and tritium autoradiography is a well-established technique for visualizing hydrogen distributions [30, 31]. Tritium autoradiography exhibits the distribution of Ag particles in a nuclear emulsion layer, decomposed of AgBr by the 18.6 keV β-ray emitted from tritium introduced into the specimen. The emulsion film is usually deposited over a thin intermediate collodion layer on the surface of a tritiated specimen. Microstructures of the metal corresponding to the distribution of Ag particles can be simultaneously revealed when the metal surface has been prepared for metallographic observation. The penetration depth of the β-ray is about 1 μm in iron-base alloys [31], and the size of AgBr particles limits the spatial resolution of autoradiography. Before coating the emulsion film, the tritiated specimens are usually exposed at room temperature to diffuse out extraneous tritium for the safety of manipulation. In this case, observed Ag particles exhibit strongly trapped sites for non-diffusive tritium.

Figure 2.16 [32] shows a tritium autoradiograph of a low-carbon ferritic steel specimen strained by 5% at 193 K. Besides accumulation along grain boundaries, the arrows A and B in Fig. 2.16 indicate a columnar distribution and a band-like assembly, respectively, while the distribution within a grain is fairly uniform when deformed at room temperature. The distributions exhibit strongly trapped tritium, and the sites well correspond to slip bands that appeared on the surface of specimens.

An alternative digital image technique is radioluminography using an imaging plate (IP) [33]. The IP technique utilizes photostimulated luminescence and has a high sensitivity with an extensive dynamic range of about five orders. The IP shows not only two-dimensional distributions but also the concentrations of tritium. However, the IP needs a long exposure time, of more than several tens hours, and the size of pixels limits the spatial resolution, currently a few tens μm.

The decomposition of AgBr in the nuclear emulsion also occurs through chemical reactions with hydrogen. The hydrogen microprint technique (HMT) is a method to reduce AgBr in the nuclear emulsion by hydrogen diffusing out from the specimen [34]. Microscopic observation of Ag particles after fixing to remove unreacted AgBr reveals the distribution of emission sites of hydrogen on the surface. Since the development process is not necessary for HMT, the spatial resolution of Ag particles is generally better than tritium autoradiography.

Fig. 2.16 Tritium
autoradiograph of a ferritic
steel tensile strained by 5%
at 193 K (−80 °C) (Aoki
et al. [32])

30 μm
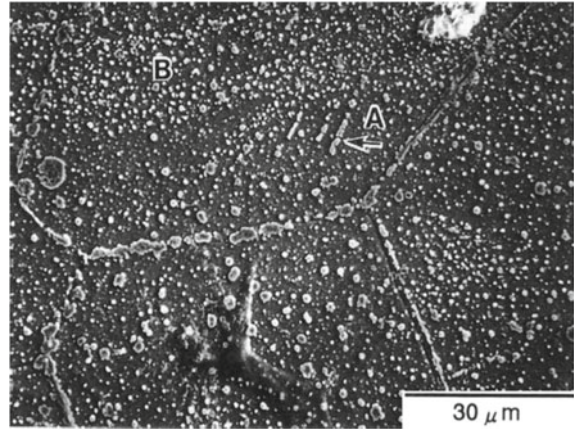
A substantial improvement of HMT has attained 0.1 μm in the spatial resolution of Ag particles and 40% in the detection efficiency of hydrogen [35]. Figure 2.17 [35] is an SEM micrograph of HMT of a ferrite-pearlite steel plate specimen of 1.8 mm in thickness, to which hydrogen was introduced from the opposite side. Preferential hydrogen evolution from the interface of cementite in the pearlite phase is clearly revealed.

Similarly, the silver decoration technique utilizes hydrogen reduction of Ag^+ ions in a solution. The specimen is immersed in a solution containing $AgNO_3$ and a small amount of KCN and then is rinsed with water and dried. Hydrogen diffusing out of the specimen adsorbs on the metal surface and reduces Ag^+ to Ag. Experiments with hydrogen-charged nickel specimens demonstrated different densities of Ag particles between neighboring grains or in annealing twins [36]. High densities along slip lines and grain boundary junctions were also revealed [36].

It must be careful that the hydrogen states detected by HMT and tritium autoradiography are not always the same in the specimen, diffusive in the former while normally non-diffusive in the latter. Observed distributions of Ag particles by HMT indicate desorption sites of hydrogen on the surface, while autoradiography shows

Fig. 2.17 Scanning electron
micrograph of hydrogen
microprint using
gelatin-hardening for a
ferrite-pearlite steel (Ichitani
et al. [35]. Reprinted with
permission from The Iron
and Steel Institute Japan)

5μm
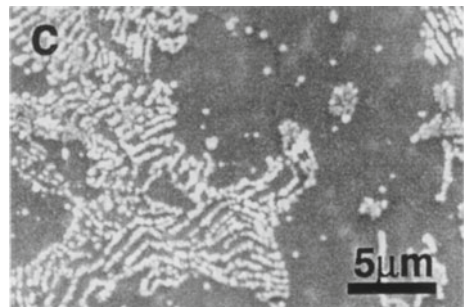
stably trapped sites of hydrogen. Accordingly, the two methods are complementary, and the use of the two together helps examine the interactions of microstructures with hydrogen.

2.3.2 Methods Using Stimulated Hydrogen Desorption

2.3.2.1 Scanning Secondary Ion Mass Spectroscopy

Scanning secondary ion mass spectroscopy (SIMS) is a high-sensitivity tool for detecting hydrogen of concentrations as low as the order of ppb, and the SIMS method is useful for detecting the distribution of hydrogen interacting with different elements. Figure 2.18 [11] shows D^-, Si^-, and P^- distributions in a cold-drawn eutectoid steel specimen subjected to a sustained-loading test in a corrosive solution containing deuterium. Sputtering the surface of the specimen with a focused primary ion beam ejects secondary ions and exhibits the distribution of elements. The mass/charge ratio of secondary ions is measured with a mass spectrometer. The primary Cs^+ beam was at 14.5 keV with a beam diameter of 30 μm, and the spatial resolution of the secondary ion image was 2 μm [37]. Accumulation of deuterium in segregation zones of Si and P is evident. Repeated sputtering of the same area by the primary ion in SIMS measurement gives a three-dimensional distribution image, and the vacuum environment enables distinction between diffusive and non-diffusive types of trapping in the specimen.

Hydrogen distributions in stress and strain fields were also exhibited with SIMS for the U-bent portion of a steel sheet [38]. The material was low-carbon martensitic steel, hydrogen-precharged by cathodic electrolysis with a current density of 1 A/m^2 in a 3% NaCl D_2O solution containing 30 g/L of NH_4SCN as a poison. For SIMS, the primary Cs^+ ion beam was at 15 keV, and an analyzing region was 600 μm $\times$ 600 μm. The change of local deuterium concentrations corresponding to a stress gradient of $\pm$ 1500 MPa over a region of 0.1 mm width was successfully detected. Kinugasa et al. also observed hydrogen localization on the shearing surface of the steel and compared it with calculated stress and strain fields [38]. Contrarily to the stress field, the deuterium distribution was hardly related to the plastic strain field.

In this case, the observed deuterium distribution exhibits redistribution of precharged deuterium after plastic work, and both intrinsic trapping defects in martensitic steel and the applied stress govern the deuterium distribution. The spatial resolution in this observation was about 0.5–1.0 μm [38]. The volume of one pixel limits the spatial resolution of SIMS, and a recent advance has reduced the one-pixel size to 50×50 nm^2. The depth of an analyzing volume to 10 nm and the ionization efficiency of 10^{-2} gives an estimated lower sensitivity limit of 50 at. ppm for iron [39].
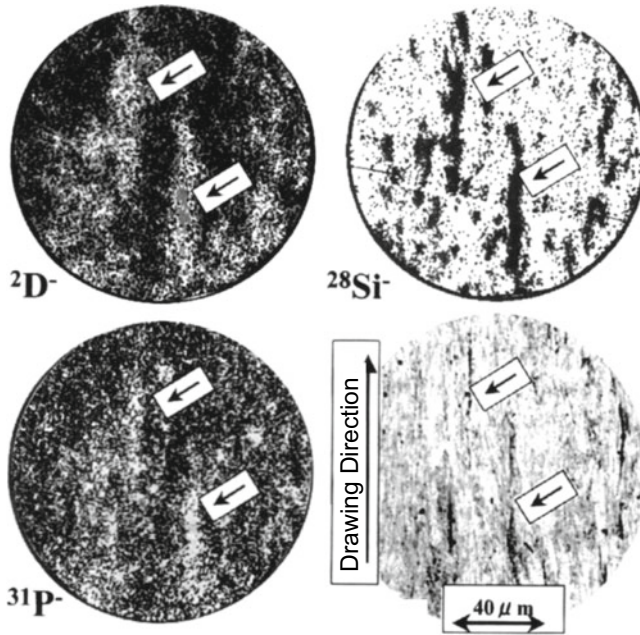
Fig. 2.18 Scanning secondary ion mass spectrometry images of cold-drawn eutectoid steel specimens dipped in a 20% NH$_4$SCN deuterium-added aqueous solution. The lower right micrograph shows microstructures (Takai et al. [11]. Reprinted with permission from The Iron and Steel Institute Japan)

2.3.2.2   Electron-Stimulated Desorption

An electron beam is an alternative to the primary ion to stimulate hydrogen desorption from the surface of metals [40, 41]. Takagi et al. succeeded in capturing hydrogen distribution images by combining a scanning electron microscope (SEM) and electron-stimulated desorption (ESD) [42]. Miyauchi et al. incorporated a hydrogen-ion detector in SEM to visualize the two-dimensional distribution of hydrogen on the surface of the specimen supplying hydrogen from the backside, naming it an "operando hydrogen microscope" [43]. The device was applied to attain a two-dimensional map of hydrogen permeation through austenitic stainless steel foil [44, 45]. Figure 2.19 [46] compares SEM and ESD-hydrogen images of Type 304 stainless steel cold-worked to 20% at room temperature. Hydrogen supply was from the bottom surface of the foil of 100 μm thickness, and the time dependence of local hydrogen permeation was recorded.

The operando hydrogen microscopy enables comparison between SEM and hydrogen images. The spatial resolution of the hydrogen map was about 1 μm [44], and different hydrogen permeation rates among austenite and martensite grains were distinct. Fine focusing of the incident electron beam is favorable to spatial resolution.
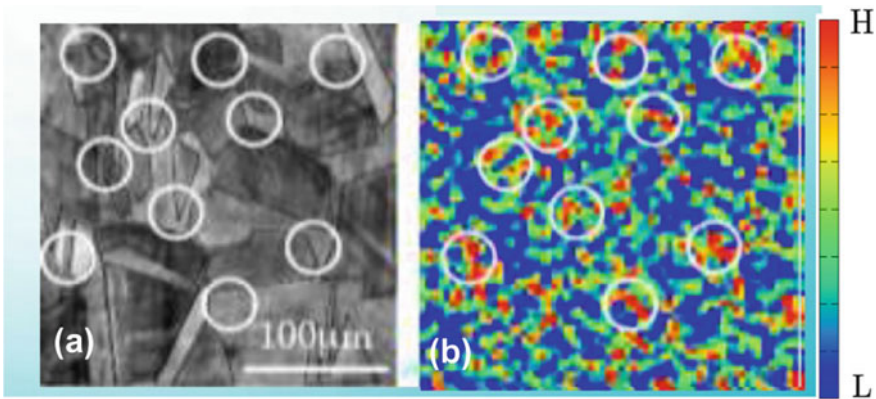
Fig. 2.19 (a) SEM and **(b)** electron-stimulated-desorption hydrogen images of Type 304 stainless steel cold-worked to 20% at room temperature. The color scale indicates the increase in number of detected ions (Miyauchi et al. [46])

On the other hand, available information is about hydrogen on the specimen surface, inevitably limiting the yield of hydrogen atoms for detection.

2.3.2.3 Atom-Probe Tomography

The Atom-Probe Tomography (APT), or the Tree-Dimensional Atom Probe (3DAP), is a method of three-dimensional imaging and chemical composition measurements at the atomic scale resolution in depth and laterally [47]. The desorption of near-surface atoms is induced by a very high electrostatic field at the tip surface, coupled with laser or voltage pulsing. Takahashi et al. introduced deuterium into the needle tip of the specimen by attaching a "deuterium charging cell" to the storage chamber of 3DAP [48]. Deuterium charging was at 523–573 K of the specimen temperature, followed by rapid cooling to keep the deuterium.

Takahashi et al. directly revealed deuterium trapping along the broad interface between needle-like carbides, TiC [48] and VC [49], and ferrite matrix in low-carbon precipitation-hardened steel. A separately conducted orientation analysis showed the broad interface on the {001} ferrite. The spatial resolution of APT is about 0.1–0.3 nm in depth and 0.3–0.5 nm laterally. On the other hand, the observing region is also limited to the needle tip, about $50 \times 50 \times 50$ nm. The focused ion beam (FIB) method is a powerful tool for preparing the specimen from a specified region in the material.

2.4 Indirect Detection of Hydrogen Distribution

2.4.1 Neutron Tomography

The response of hydrogen to external excitations is generally very weak, but neutron interacts strongly with proton. Neutron tomography (NT) is a technique to produce a three-dimensional image of the absorbance of neutrons in materials. Griesche et al. applied NT to exhibit hydrogen distributions around blisters and cracks formed in ferritic iron by electrochemical hydrogen charging [50]. The spatial resolution was about 20–30 μm. Precipitation of molecular hydrogen gas in cracks and a hydrogen-enriched zone of 50 μm wide surrounding cracks were detected. Hydrogen also accumulated at the sample surface, having the highest concentration in blistered areas, and the hydrogen accumulation around the cracks could be removed like diffusive hydrogen by mild temperature treatment.

2.4.2 Scanning Kelvin Prove Microscopy

Scanning Kelvin Probe Microscopy (SKPM) measures two-dimensional distributions of contact potential difference (CPD) between the tip and the metal sample, commonly using the vibrating capacitor method [51]. The CPD corresponds to the work function of the sample and determines a long-range electrostatic force between the tip and the sample. Scanning Kelvin Probe Force Microscope (SKPFM) combines Kelvin probe method and the atomic force microscope (AFM) in non-contact mode, making it possible to plot the potential map of a surface with a lateral resolution in the nanometer range [51, 52]. Hydrogen adsorbed on metals can significantly change their work function.

Senöz et al. observed, using SKPFM, time-dependent changes in the local surface potential of polycrystalline metal membranes associated with the hydrogen permeation from the bottom [53]. For Pd of 100 μm thickness, a difference in the evolution appeared between the (111) and (001) grain orientations in the potential change. For ferrite/austenite duplex-phase steel of 60 μm thickness, a striking contrast appeared on the ferrite as compared to the austenite [53], consistent with a higher hydrogen diffusivity in ferrite.

Krieger et al. observed the time evolution of the potentials during the SKPFM imaging for hydrogen-precharged 5% Ni ferritic alloys [54]. Three states of the alloy, i.e., annealed, cold-rolled 10 → 1 mm, recrystallized, were prepared, and hydrogen was precharged in a mild condition of cathodic electrolysis in 0.1 M NaOH at −1 V SHE. SKPFM revealed the effects of the three treatments on potential changes to appear only around borders of oxide inclusions, while TDA of precharged hydrogen exhibited implied substantial differences in the trapping of hydrogen by the three treatments.

Detecting time-dependent local hydrogen desorption with SKPFM was also conducted by Koyama et al. for a Fe–18Mn–1.2C (wt%) steel [55]. The steel was tensile-strained to 30% to produce deformation twins, and hydrogen was introduced by cathodic electrolysis in a 0.9 M H_2SO_4 aqueous solution containing $3 \; g \cdot L^{-1}$ of NH_4SCN at a voltage of -700 mV versus Ag/AgCl for 30 min. SKPM gives topographic information and discerns the deformation twin formation. The potential at deformation twins was lower than the average potential of the matrix, and the difference increased with exposure time until 67 h and then turned to recover. A suggested reason for the difference was the local hydrogen diffusivity, twins acting as the longer-storage region of hydrogen [55].

The direct information from SKPMF is the local distribution of the surface potential, affected by many factors, such as topographic features, residual stress, surface corrosion products, besides compositions and microstructures of the material. The spatial resolution is basically in the nanometer range in principle, but sharp images of grain boundaries, inclusion borders, and twin interfaces were not exhibited in the studies cited above.

References

1. J.R.G. da Silva, S.W. Stafford, R.B. McLellan, J. Less Common Metals **49**, 407–420 (1976)
2. O.D. Gonzalez, Trans. Metall. Soc. AIME **245**, 607–612 (1969)
3. A.J. Kumnick, H.H. Johnson, Metall. Trans. A **6A**, 1087–1091 (1975)
4. K. Yamakawa, T. Tsuruta, S. Yoshizawa, Boshoku-Gijutsu **30**, 443–449 (1981)
5. R.A. Oriani, P.H. Josephic, Acta Metall. **27**, 997–1005 (1979)
6. K. Yamakawa, in *Advances in Delayed Fracture Solution* (Iron and Steel Institute Japan, Tokyo, 1997), pp. 77–81
7. J.P. Hirth, B. Carnahan, Acta Metall. **26**, 1795–1803 (1978)
8. R.B. McLellan, Acta Metall. **27**, 1655–1663 (1979)
9. D.N. Beshers, Acta Metall. **6**, 521–523 (1958)
10. Y. Sugiyama, K. Takai, Acta Mater. **208**, 116663 (2021)
11. K. Takai, J. Seki, Y. Homma, Tetsu-to-Hagané **81**, 1025–1030 (1995)
12. A. McNabb, P.K. Foster, Trans. Metall. Soc. AIME. **227**, 618–627 (1963)
13. T. Kasuya, M. Fuji, J. Appl. Phys. **83**, 3039–3048 (1998)
14. P.A. Redhead, Vacuum **12**, 203–211 (1963)
15. W.Y. Choo, J.Y. Lee, Metall. Trans. A **13A**, 135–140 (1982)
16. J.L. Lee, J.Y. Lee, Metall. Trans. A **16A**, 468–471 (1985)
17. K. Ono, M. Meshii, Acta Metall. Mater. **40**, 1357–1364 (1992)
18. K. Takai, G. Yamauchi, M. Nakamura, M. Nagumo, J. Jpn. Inst. Metals **62**, 267–275 (1998)
19. H.E. Kissinger, Analyt. Chem. **29**, 1702–1706 (1957)
20. M. Nagumo, K. Ohta, H. Saitoh, Scripta Mater. **40**, 313–319 (1999)
21. R.A. Oriani, Acta Metall. **18**, 147–157 (1970)
22. K. Takai, R. Watanuki, ISIJ Int. **43**, 520–526 (2003)
23. A. Turnbull, R.B. Hutchings, D.H. Ferriss, Mater. Sci. Eng. **A238**, 317–328 (1997)
24. T. Yamaguchi, M. Nagumo, ISIJ Int. **43**, 514–519 (2003)
25. M. Enomoto, D. Hirakami, T. Tarui, ISIJ Int. **46**, 1381–1387 (2006)
26. K. Ebihara, T. Suzudo, H. Kaburaki, K. Takai, S. Takebayashi, ISIJ Int. **47**, 1131–1141 (2007)
27. Y. Sato, K. Fujita, H. Suzuki, K. Takai, Y. Hagiwara, K. Maejima, N. Miyabayashi, CAMP ISIJ **21**, 1375 (2008)

28. N. Abe, H. Suzuki, K. Takai, N. Ishikawa, H. Sueyoshi, Mater. Sci. Tech. Conf. Exhibition 2011, MS & T'11, pp. 1277–1284
29. B.G. Pound, G.A. Wright, R.M. Sharp, Acta Metall. **35**, 263–270 (1987)
30. P. Lacombe, M. Aucouturier, J. Chéne, in *Hydrogen Embrittlement and Stress Corrosion Cracking*, ed. by R. Gibara, R.F. Hehemann (ASM, Metals Park OH, 1984), pp. 79–102
31. J. Chéne, A.M. Brass, in *Hydrogen Effects in Materials*, ed by A.W. Thompson, N.R. Moody (TMS, Warrendale PA 1996), pp. 47–59
32. M. Aoki, H. Saito, N. Mori, Y. Ishida, M. Nagumo, J. Jpn. Inst. Metals **58**, 1141–1148 (1994)
33. H. Saitoh, T. Hishi, T. Misawa, T. Ohnishi, Y. Noya. T. Matsuzaki, T. Watanabe, J. Nucl. Mater. **258/263**, 1404–1408 (1998)
34. J. Overjero-Garcia, J. Mater. Sci. **20**, 2623–2629 (1985)
35. K. Ichitani, M. Kanno, S. Kuramoto, ISIJ Int. **43**, 496–504 (2003)
36. T. Shober, C. Dieker, Metall. Trans. A **14A**, 2440–2442 (1983)
37. K. Takai, J. Seki, G. Yamauchi, Y. Homma, J. Japan Inst. Metals **58**, 1380–1385 (1994)
38. J. Kinugasa, S. Yabu, K. Shibata, T. Hiramatsu, M. Kawamori, F. Yusei, ISIJ Int. **61**, 1091–1098 (2021)
39. M. Kawamori, S. Yabu, The 190th Committee on Hydrogen Function Analyses in Materials (2016)
40. T.E. Madey, J.T. Yates Jr., J. Vac. Sci. Technol. **8**, 525–555 (1971)
41. K. Ishikawa, M. Yoshimura, K. Ueda, Y. Sakai, Rev. Sci. Instr. **68**, 4103–4106 (1997)
42. T. Takagi, T. Gotoh, Surf. Sci. **287**(288), 361–365 (1993)
43. N. Miyauchi, T. Iwasawa, T. Yakabe, M. Tosa, T. Shindo, S. Takagi, A.N. Itakura, Appl. Surf. Sci. **492**, 280–284 (2019)
44. N. Miyauchi, T. Iwasawa, Y. Murase, T. Yakabe, M. Kitajima, S. Takagi, T. Akiyama, S. Aoyagi, A.N. Itakura, Appl. Surf. Sci. **527**, 146710 (2020)
45. A.N. Itakura, N. Miyauchi, T. Iwasawa, Y. Murase, T. Yakabe, M. Kitajima, Sci. Rep. **11**, 8553 (2021)
46. N. Miyauchi, K. Hirata, Y. Murase, H.A. Sakaue, T. Yakabe, A.N. Itakura, T. Gotoh, S. Takagi, Scripta Mater. **144**, 69–73 (2018)
47. W. Müller, J.A. Panitz, S.B. McLane, Rev. Sci. Instruments **39**, 83–86 (1968)
48. J. Takahashi, K. Kawakami, Y. Kobayashi, T. Tarui, Scripta Mater. **63**, 261–264 (2010)
49. J. Takahashi, K. Kawakami, Y. Kobayashi, Acta Mater. **153**, 193–204 (2018)
50. A. Griesche, E. Dabah, T. Kannengiesser, N. Kardjilov, A. Hilger, I. Manke, Acta Mater. **78**, 14–22 (2014)
51. M. Nonnenmacher, M.P. O'Boyle, H.K. Wickramasinghe, Appl. Phys. Lett. **58**, 2921–2923 (1991)
52. S. Evers, C. Senoz, M. Rohwerder. Sci. Technol. Adv. Mater. **14**, 014201 (2013)
53. C. Senöz, S. Evers, M. Stratmann, M. Rohwerder, Electrochem. Commun. **13**, 1542–1545 (2011)
54. W. Krieger, S.V. Merzlikin, A. Bashir, A. Szczepaniak, H. Springer, M. Rohwerder, Acta Mater. **144**, 235–245 (2018)
55. M. Koyama, A. Bashir, M. Rohwerder, S.V. Merzlikin, E. Akiyama, K. Tsuzaki, D. Raabe, J. Electrochem. Soc. **162**, C638–C647 (2015)